



# The Effect of Asymmetry on Strain Distribution, Microstructure and Texture of Multilayer Aluminum Composites Formed by Roll-Bonding

D. C. C. Magalhães<sup>1</sup>, J. B. Rubert<sup>2</sup>, O. M. Cintho<sup>3</sup>, V. L. Sordi<sup>1</sup> and A. M. Kliauga<sup>1\*</sup>

<sup>1</sup>Materials Engineering Department, Federal University of São Carlos (UFSCar), São Carlos, Brazil, <sup>2</sup>Mechanical Engineering Department, Federal University of São Carlos (UFSCar), São Carlos, Brazil, <sup>3</sup>Materials Engineering Department, State University of Ponta Grossa (UEPG), Ponta Grossa, Brazil

AA1050/AA7050 multilayered composite sheets with a proportion of 1:1 were produced by Accumulative Roll Bonding (ARB) and Asymmetric Accumulative Roll-Bonding (AARB), using up to 8 cycles and intermediate annealing treatments at 500°C. The main purpose was to produce one composite sheet with high strength and moderate ductility, taking advantage of the mechanical properties of these aluminum alloys. Microstructural features were investigated in order to evaluate the potential to achieve a refined microstructure and the development of structural patterns. The strain distributions as a function of friction and asymmetry were simulated by finite element analysis. Texture was evaluated by X-ray diffraction and electron backscatter diffraction. A continuous layer pattern was obtained by ARB, up to 6 cycles but after 8 cycles shear bands fragmented the harder layers. In the early AARB cycles, the bending and necking of the AA7050 layers yielded a wavy-pattern. The shear strain in the AARB process has a strong influence on achieving a wavy-pattern, more than the flow stress differences of the alloys in the composite. Shear texture increased with the degree of the layers' discontinuity. Different sources of shear contributed to the formation of microstructural patterns: the shear due to asymmetry, the frictional shear at roll-sheet interface and at the central layer interface and the shear at the layers' interface. In addition, the ARB process achieved a better interfacial adhesion at the middle interface and higher strength and elongation than the AARB process.

**Keywords:** accumulative roll-bonding, asymmetry, aluminum alloys, texture, strain distribution analysis

## INTRODUCTION

Severe Plastic Deformation (SPD) techniques have attracted growing interest because they can induce an intense grain refinement. Among SPD techniques, Accumulative Roll-Bonding (ARB) is suitable to produce flat products, including multilayered composite sheets, while taking advantage of the industrial rolling plants (Tsuji et al., 2003; Li et al., 2008; Ruppert et al., 2013). In addition, ARB can successfully produce structures with sub-micrometric or nanometric grain sizes, thus increasing strength, hardness, formability, fatigue resistance and other properties (Jamaati and Toroghinejad, 2011; Su et al., 2013; Fattah-Alhosseini et al., 2017; Rahmatabadi et al., 2017).

A critical step in the ARB process is to achieve a strong interface. To improve the diffusion-assisted bonding, the breakdown of thin oxide films at the sheet's surfaces is important, which can be

## OPEN ACCESS

### Edited by:

Zhenggang Wu,  
Hunan University, China

### Reviewed by:

Lihong Su,  
University of Wollongong, Australia  
Yuan Li,  
Oak Ridge National Laboratory (DOE),  
United States

### \*Correspondence:

A. M. Kliauga  
kliauga@ufscar.br

### Specialty section:

This article was submitted to  
Structural Materials,  
a section of the journal  
Frontiers in Materials

**Received:** 28 August 2020

**Accepted:** 24 November 2020

**Published:** 18 December 2020

### Citation:

Magalhães DCC, Rubert J B,  
Cintho OM, Sordi VL and Kliauga AM  
(2020) The Effect of Asymmetry on  
Strain Distribution, Microstructure and  
Texture of Multilayer Aluminum  
Composites Formed by Roll-Bonding.  
Front. Mater. 7:600162.  
doi: 10.3389/fmats.2020.600162

made by compression and/or shear (Li et al., 2008; Jamaati and Toroghinejad, 2011). The shear strain might be introduced into the roll-bonding using the asymmetric rolls, then the process is called Asymmetric Accumulative Roll-Bonding (AARB). The AARB is able to produce ultrafine-grained structures, and thus enhance mechanical response, as reported in earlier works (Mi et al., 2011; Wang et al., 2012; Ng et al., 2013; Wierzba et al., 2015; de Godoi et al., 2020; Magalhães et al., 2020b). However, it remains unclear if the AARB really helps to achieve a stronger interface for Al-based multilayered composites. Only a few investigations have been performed using other dissimilar systems processed by both ARB and AARB (Ng et al., 2013; Wierzba et al., 2015; Mendes et al., 2017; Magalhães et al., 2020a) but no study has demonstrated if the interfacial integrity and tensile properties were improved.

Sometimes, during the roll-bonding of dissimilar alloys, plastic instabilities take place due to different flow stresses and distinct macrostructural configurations can be developed. A multilayered composite with a flat-pattern structure is achieved when the harder layer preserves its continuity (Anne et al., 2017). In contrast, a wavy-pattern structure with fragments of the harder phase embedded into the soft matrix is formed if the harder layers neck and rupture during the roll-bonding (Rahmatabadi et al., 2018; Wang et al., 2018). These pattern configurations play an important role in the mechanical behavior, due to limiting the damage initiation in the composite during the deformation (Kulagin et al., 2019). Therefore, the investigation of the influence of the roll-bonding technique on the pattern development is important to control the manufacturing process. So far, very little attention has been paid to the role of macrostructural configurations produced by roll-bonding processes in an Al-based multilayered composite sheet and their effects on the strain distribution, texture and tensile behavior.

Concerning the mechanical behavior, the development of metallic composites with bimodal grain size distribution has emerged as an alternative application of SPD techniques to enhance the strength-ductility pair (Valiev, 2004; Wang and Ma, 2004; Kumar et al., 2016). In this case, the bimodal grain structures are composed by both submicrometric and/or nanometric grains and coarser grains: the former confer strength, and the latter assist the strain-hardening capacity (Zhao et al., 2006; Höppel et al., 2010; Huang et al., 2015; Samaee et al., 2016). Thus, Naseri's group (Naseri et al., 2016) states that a bimodal grain structure in an AA2024 alloy can be achieved combining prior roll-bonded sheets with annealed strips via ARB, which resulted in a total elongation of ~10%. In another investigation, Ebrahimi and co-authors (Ebrahimi et al., 2018) produced via ARB at 400 °C sheets of AA1050/Al-12Zn-3Mg-2.5Cu that achieved an ultimate tensile strength of 434 MPa with 23% total elongation.

In the present work, the AA7050 alloy was used as a hard phase and combined with AA1050 as a ductile matrix in a composite sheet. The AA7050 is a high-performance alloy due to remarkable amounts of precipitates, and then presents low tendency to recrystallization and grain growth, even in the mechanical processing at high temperature (>400 °C)

(Rometsch et al., 2014). In contrast, the commercially pure aluminum, namely AA1050, has excellent ductility and low strength. The dissimilar properties of these materials could produce a multilayer composite with technological applications, in which the harder phase would present a finer grain size, while the softer matrix would present coarse grains. Two rolling configurations (ARB and AARB) were applied in order to produce different macrostructural configurations and to elucidate the effect of shear strain in the pattern formation, texture and tensile properties.

## MATERIALS AND METHODS

Commercial AA1050 (0.185% Fe, 0.081% Si and Al balance) and AA7050 (6.46% Zn, 2.39% Mg, 3.49% Cu and Al balance) aluminum alloys were used in this work. In order to characterize the mechanical behavior of the two alloys at the processing temperature, isothermal hot compression tests using cylinder samples with 6 mm of diameter and 8 mm of height were carried out on samples of AA1050 and AA7050 alloy in annealed and overaged states, respectively. The specimens were heated with a heating rate of 10 °C s<sup>-1</sup> and held for 5 min at the deformation temperature prior to compression tests. The isothermal tests were performed at room temperature, 300, 400, and 500 °C. All samples were tested in an Instron 5500 machine under an initial strain rate of 1.0 × 10<sup>-3</sup> s<sup>-1</sup> up to a height reduction of 50%, which corresponds to ~0.69 of true plastic strain.

Plates of AA1050 Al alloy with a thickness of 1 mm were annealed at 500 °C for 10 min. The AA7050 Al alloy in an overaged state (T7451) was rolled at 400 °C to a thickness of 2 mm, producing a recovered and overaged microstructure. This initial rolling was performed in a conventional mill for both alloys.

The initial bonding set was produced positioning one AA7050 sheet with 50 × 70 × 2 mm between two AA1050 sheets with 50 × 70 × 1 mm, maintaining a volume proportion of 1:1. The ARB processing was performed in a conventional mill operating at 61 rpm. The AARB deformation cycles were performed in an asymmetric rolling mill with the roll diameter ratio of 1:1.5, operating at 23 rpm. The roll's surfaces were grooved in order to achieve a high friction coefficient and no lubricant was applied. Before the roll-bonding, the sheets were wire-brushed to increase the roughness followed by ultrasonic degreasing in ethanol. The initial stacks were preheated for 5 min at 500 °C. For both routes a thickness reduction of 50% in a single pass was applied. The mills were kept at room temperature and the rolling was performed within a temperature gradient. Immediately after rolling, the sheets were water quenched. The roll-bonded sheet was cut in half, wire-brushed, cleaned, stacked again to produce a new stack, and pre-heated at 500 °C (intermediate annealing step) and then this processing sequence was repeated up to 8 cycles (8X).

The crystallographic texture of the sheets was determined through X-ray diffraction on a Philips X'Pert MPD diffractometer using Co-K<sub>α</sub> radiation with the Schulz method, at the LNNano Synchrotron National Laboratory in Campinas—SP, Brazil. The pole figures of all samples were measured at 1/4 and 3/4 of the

sheet thickness counting from the upper surface. At the State University of Ponta Grossa (UEPG), the mesotexture was measured by means of EBSD using a TESCAN-FEG MIRA 3 microscope, equipped with an Oxford Instrument EBSD detector and operated at 20 kV. EBSD data were collected with a step size in the range of 0.2  $\mu\text{m}$  taken on the RD-ND plane. All the sample surfaces were electropolished using a solution with 160 mL distilled water, 800 mL ethanol and 60 mL perchloric acid at  $\sim 10^\circ\text{C}$  for 20 s with a voltage of 25 V. The evaluation of the texture and mesotexture obtained by X-ray diffraction and EBSD was analyzed using the ATEX software (Beausir and Fundenberger, 2017).

The finite element simulation (FES) was performed using the software package DEFORM 3D<sup>TM</sup>. The same geometrical parameters of the experimental rolling mills were applied. The initial dimensions of the sets were 20  $\times$  35 mm with a total thickness of 4 mm; a symmetry restriction in the middle RD-ND (rolling direction–normal direction) plane was imposed. The thickness was subdivided into eight hexahedral elements for both AR and AARB simulations. Sheets were considered as being elastoplastic and the rolls perfectly rigid bodies. A triaxial deformation model was applied and the material behavior was described by the interpolation of stress–strain curves from the software databank, which were in agreement with experimental data. A shear friction coefficient  $m$  of 0.9 was applied at the rough roll-sheet interface for AARB and an  $m$  of 0.45 was applied to simulate a polished surface in the ARB process. Between the layer interface a sticking condition was applied and the shear friction coefficient at the central interface was assumed to be 0.9.

## RESULTS

The stress–strain curves from the compression experiment were fitted using the Johnson–Cook (JC) model of plastic flow:

$$\sigma = (A + B\epsilon^n) \left( 1 + C \ln \frac{\dot{\epsilon}}{\dot{\epsilon}_0} \right) (1 - T^{*m})$$

where  $A$ ,  $B$  and  $C$  are material constants,  $n$  is the hardening exponent,  $\dot{\epsilon}$  the strain rate,  $\dot{\epsilon}_0$  the strain rate of reference ( $0.001 \text{ s}^{-1}$ ) and  $m$  the softening exponent due to temperature increase.  $T^*$  is given by:

$$T^* = \frac{T - T_r}{T_m - T_r}$$

where  $T$  is the working temperature,  $T_r$  the room temperature and  $T_m$  the melting temperature. The calculated parameters for the AA1050 and AA7050 alloys are given in **Table 1**. **Figure 1** shows the true stress–true strain experimental curves at  $500^\circ\text{C}$ , the fitted curves using the JC model and the expected curves for a strain rate of  $20 \text{ s}^{-1}$ , which is the actual strain rate of the rolling process. Using the data from the compression experiments, the JC fit and data from the literature (Abo-Elkhier, 2004; Chen et al., 2016), good estimates for the saturation stress during the rolling process

**TABLE 1** | Constants used in the JC equation.

Alloy	A	B	n	C	m
AA1050	30	65	0.1	0.014	0.35
AA7050	200	100	0.2	0.016	0.35

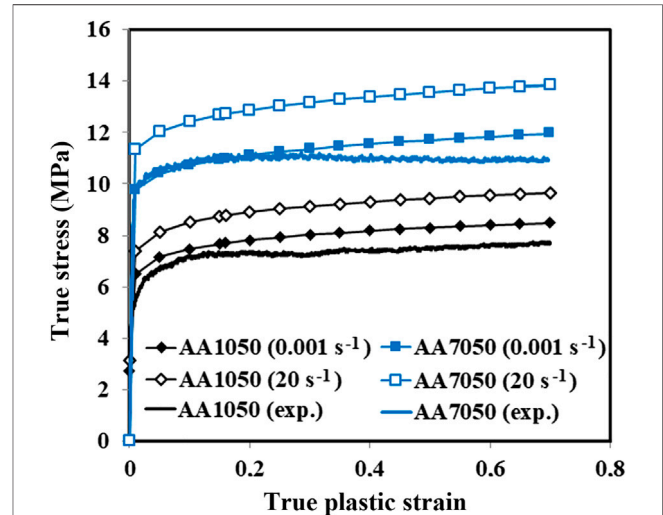


**FIGURE 1** | Experimental and calculated flow stress curves (JC) for the AA1050 and AA7050 alloys at  $500^\circ\text{C}$  for the strain rates of  $0.001$  and  $20 \text{ s}^{-1}$ .

for the AA1050 and the AA7050 aluminum alloys were 10 and 14 MPa, respectively. This small difference was observed because at  $500^\circ\text{C}$  most solutes that harden the AA7050 alloy by precipitation are in solid solution.

The equivalent von Mises strain ( $\epsilon_{\text{ARB}}$ ) for a single ARB pass is given by:

$$\epsilon_{\text{ARB}} = \frac{2}{\sqrt{3}} \ln \left( \frac{h_i}{h_f} \right)$$

where  $h_i$  and  $h_f$  are, respectively, the initial (4 mm) and final (2 mm) sheet thicknesses, and thus a single ARB cycle provides a total of  $\epsilon_{\text{ARB}} = 0.8$ .

The equivalent von Mises strain ( $\epsilon_{\text{AARB}}$ ) in one AARB cycle (Sidor et al., 2008) was expressed by:

$$\epsilon_{\text{AARB}} = \frac{\sqrt{2}}{3} \left\{ 6 \left[ \ln \left( 1 - \frac{(h_i - h_f)}{h_i} \right) \right]^2 + \frac{6}{(h_i + h_f)^2} \times \left[ R_1 \cos^{-1} \left( \frac{2R_1 - (h_i - h_f)}{2R_1} \right) - R_2 \cos^{-1} \left( \frac{2R_2 - (h_i - h_f)}{2R_2} \right) \right]^2 \right\}^{1/2}$$

where  $R_1$  and  $R_2$  are the radius of the upper and bottom rolls. For the mill used in the present work,  $R_1 = 66.0 \text{ mm}$  and  $R_2 = 44.0 \text{ mm}$  for all cycles. Each AARB cycle resulted in a total equivalent von Mises strain of 0.9 (12.5% higher than ARB).

Thus, both roll-bonding techniques applied enough strain to achieve the saturation stress and enable recrystallization and/or recovery of the microstructure. Intermediate annealing also achieved a steady state flow. Therefore, the process as applied in this work should not produce accumulative strains as in room temperature roll-bonding.

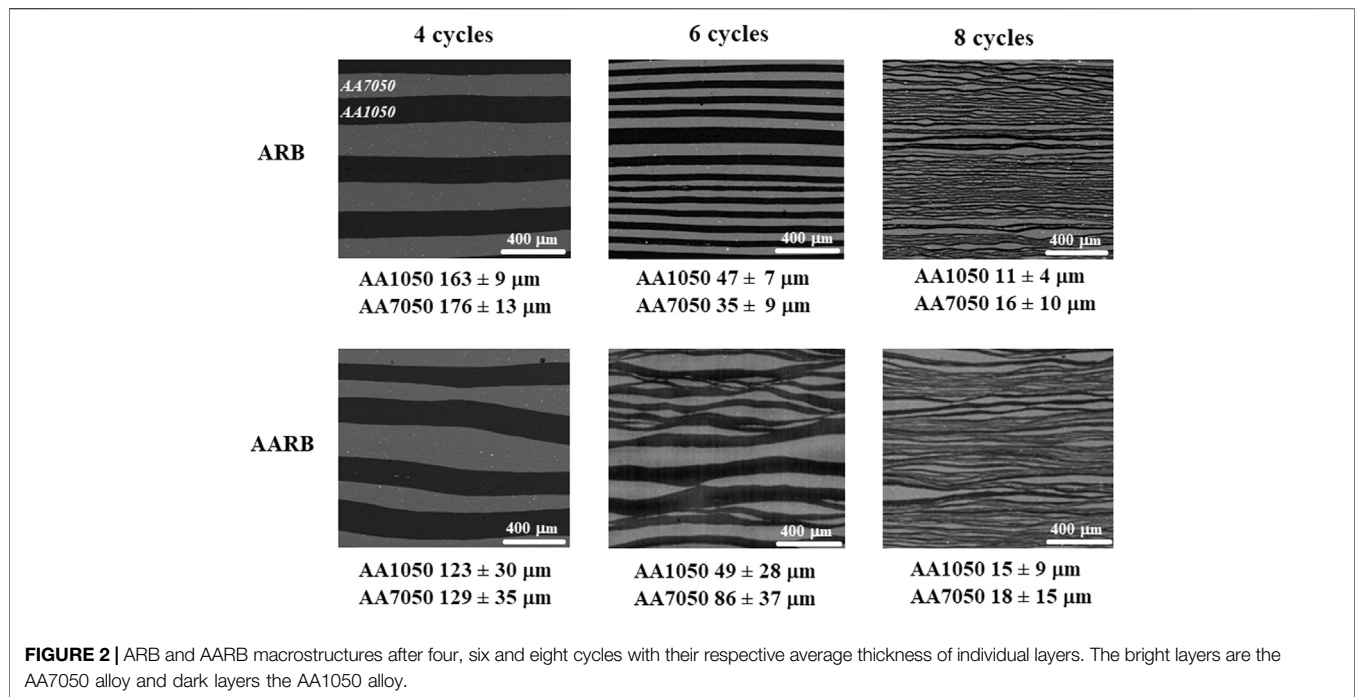


**Figure 2** shows the obtained macrostructures after four, six and eight cycles obtained with backscattered electron contrast. The bright layers are the AA7050 alloy and dark layers the AA1050 alloy. The average thickness values and their mean standard deviation are presented below the macrostructures. They were measured using at least 150 layers in five fields at the same magnification, and the thicknesses were taken in different points in the layers, including the necking regions. It can be observed that the AARB samples presented shear banding since the early cycles, which promoted necking and fracture of the AA7050 layers and yielded a wavy-pattern. For ARB, the presence of shear banding was evident only after 8 cycles. In addition, thickness gradients developed after successive stacking, because compression was higher close to the rolls for both processes. The average layer thickness also presented higher deviation for the AARB variant, as shown in **Figure 2**.

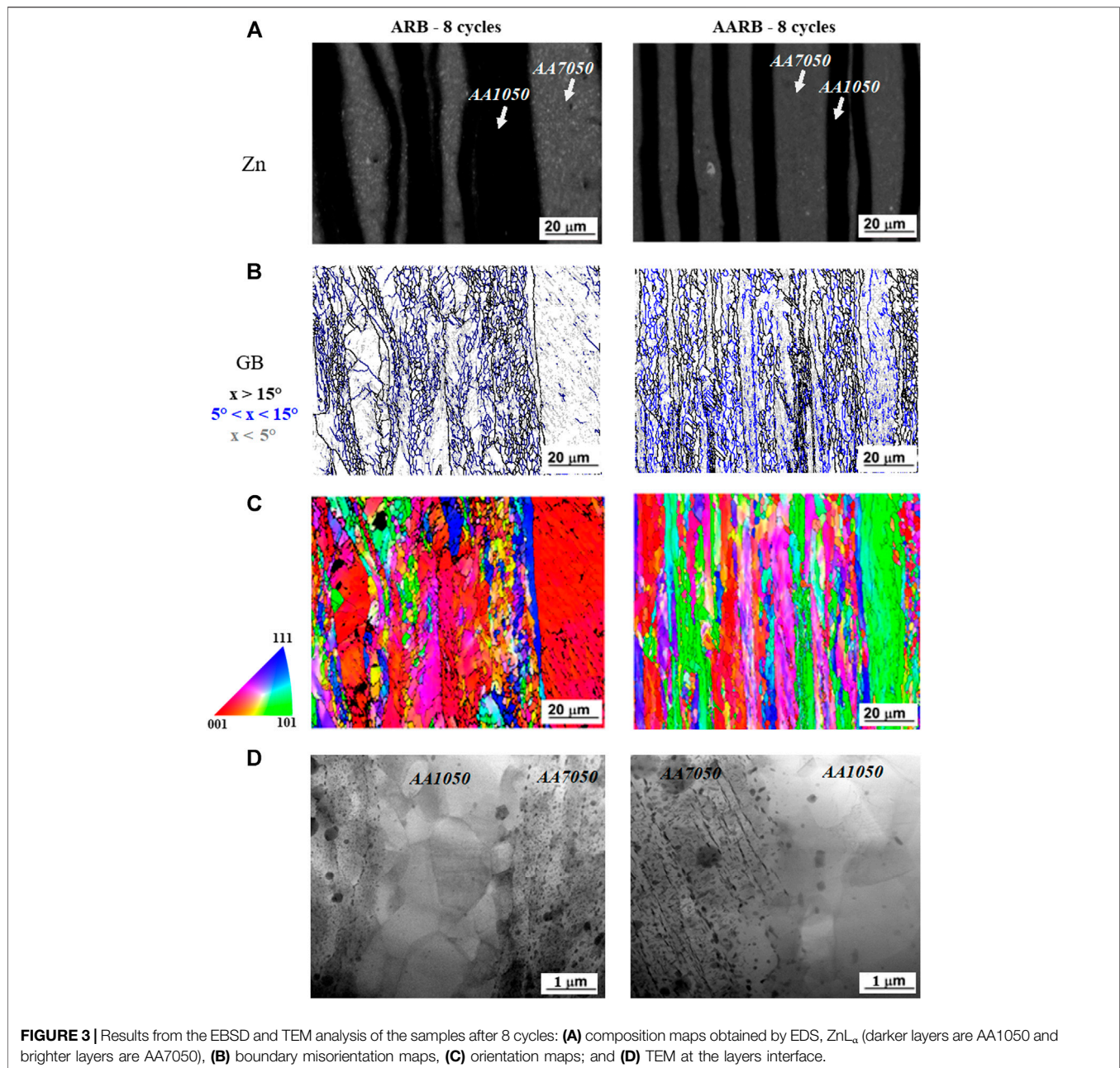
The difference of flow stress and hardening behavior of the layers is one of the possible causes for the localized deformation and partitioning of the AA7050 layers that yield to the wavy-pattern (Yazar et al., 2005; Reihanian and Naseri, 2016). However, only differences in flow stress at 500°C are not able to explain the development of the wavy-pattern.

**Figure 3** shows the results from the EBSD mapping after 8 bonding cycles. The element mapping in **Figure 3A** is presented to facilitate the identification of the individual layers. The amount of dislocation arrangements with misorientation smaller than five degrees in the AA7050 alloy was higher than in the AA1050 alloy (see **Figure 3B**), indicating that the diffusion of alloying elements interferes in the dislocation glide at this temperature and it was associated with the dynamic strain aging (DSA) commonly observed in the AA7050 alloy at high temperatures that limited the recovery process. The AA1050 layers show partial recrystallization and a

higher density of high angle grain boundaries (HAGBs). The orientation maps (**Figure 3C**) show a coarse-grained structure for the AA7050 alloy and a partially recrystallized microstructure for the AA1050 alloy. The AA7050 layers present a high density of secondary phase particles as shown in **Figure 3D**, which dissolve partially at the intermediate annealing and re-precipitate during cooling after rolling. The element mapping and the TEM (see **Figure 3D**) shows that interdiffusion of the alloying elements was not enough to cause precipitation in the AA1050 layers.

Another hypothesis to the difference in microstructural pattern is the different intensity of shear strain imposed in the two experimental configurations. The finite element simulation of the first bonding cycle was performed to clarify this aspect. **Figure 4** shows the strain profiles along the sheet thickness for three stacking configurations using the symmetric and asymmetric mills: a single sheet, two sheets of the same material, and three sheets with two different materials.

**Figure 4A** compares the influence of the roll-sheet friction for a single phase (AA1050 alloy). At a thickness reduction of 50%, the major strain component was compression. The shear strain was related to the frictional forces at the roll-sheet interface and the maximal intensity was located at these interfaces. In the symmetric case, the shear assumed maximal intensity close to the rolls and its signal inverts from positive values at the upper surface to negative values at the bottom surface; in the sample center the shear was null. If the friction was increased, the shear gradient increased. When the asymmetry was introduced, the gradient was shifted to the positive sign, and the intensity of shear at the sample center was not null. It was evident from the comparison between symmetric and asymmetric conditions with variable friction coefficients that this last parameter had greater influence over the shear imposed in the process. For the



experimental configuration, the AARB was performed in a high friction regime whereas the ARB in the low friction regime.

**Figure 4B** presented the bonding of two layers of the same composition (AA1050 or AA7050). The profile of the compression component was very similar to the one obtained rolling a single sheet, but the shear component presented a discontinuity at the boundary, which indicated that an additional shear gradient was created at the bonding interface. Moreover, the net shear at the interface for ARB was null, whereas for AARB a positive shear was created at the interface.

Finally, **Figure 4C** shows the three-layer configuration used in the first bonding cycle: AA1050/AA7050/AA1050. In this case, the friction coefficient at the layer interface was 0.9; the ARB was

treated as a low friction case and the AARB as high friction. The central layer accumulates half the strain as the softer layers in the case of high friction. For low friction these differences decreased. The compression components were very similar for the two variations. The major differences were in the shear components. With low friction, the main variation was found at the layer interface, but it concentrated in the AA1050 layer. For AARB, a shear gradient was also formed in the central layer and both roll-sheet interfaces had shear of the same sign.

For the last simulation experiment, it was observed that a strain gradient along the rolling direction was also present. **Figure 5** shows maps of the variation of compression and shear components for ARB (**Figure 5A**) and AARB (**Figure 5B**). The wavy-pattern was

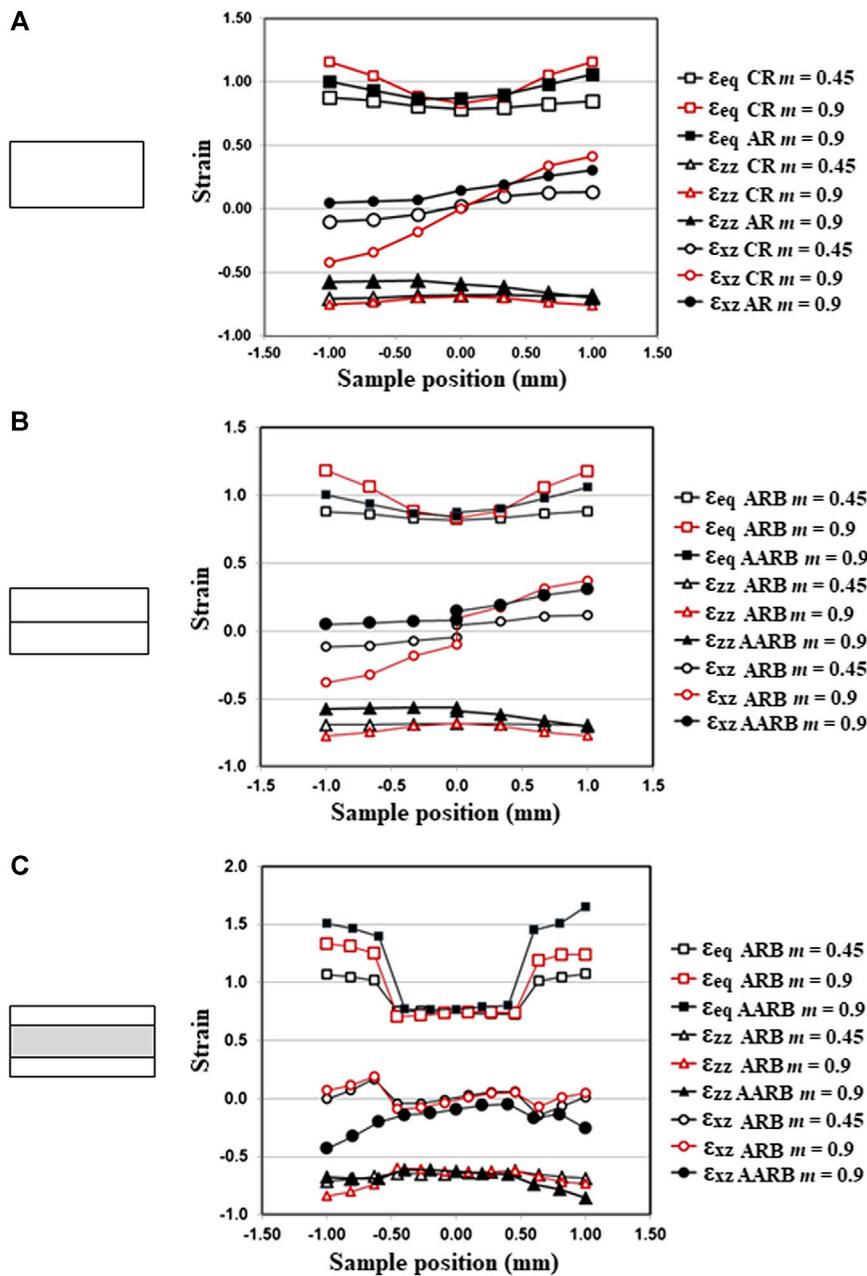


**FIGURE 4** | Strain components: equivalent strain ( $\epsilon_{eq}$ ), compressive component ( $\epsilon_{zz}$ ) and shear component ( $\epsilon_{xz}$ ). Influence of the friction coefficient at the roll-sheet interface  $m = 0.9$  or  $m = 0.45$ , sticking condition  $m = 0.9$  at the layers interface and  $T = 500^\circ\text{C}$ . **(A)** A single layer of AA1050 or AA7050, **(B)** two layers of the same material (AA1050 or AA7050), and **(C)** three layers in the sequence AA1050/AA7050/AA1050.

associated with this strain gradient: the heterogeneous strain distribution was caused by the formation of macroscopic shear bands, and the stronger the shear across the AA7050 layers, the more intense the thickness variation. **Figure 5** also shows how the strain intensity mismatch due to interfacial friction and strain hardening created the shear gradients at the interfaces of the layers that will nucleate the shear bands in subsequent cycles.

The microstructural feature that is most sensitive to the strain distribution is the crystallographic texture. Therefore, the texture

measurements of the experimental samples show to which extent the simulations may be used to interpret the bonding process. **Figure 6** shows the  $\{111\}$  pole figures for a thickness reduction of 50% of AA1050 alloy in conventional rolling (CR) and AR, at room temperature, as a reference and experimental evidence of the difference between the two processes. The expected rolling texture for CR (containing Bs  $\{011\}\langle 211\rangle$ , Cu  $\{112\}\langle 111\rangle$  and S  $\{123\}\langle 634\rangle$  components) was obtained. The AR presents a mixed character with a rotation around the transverse axis yields the B

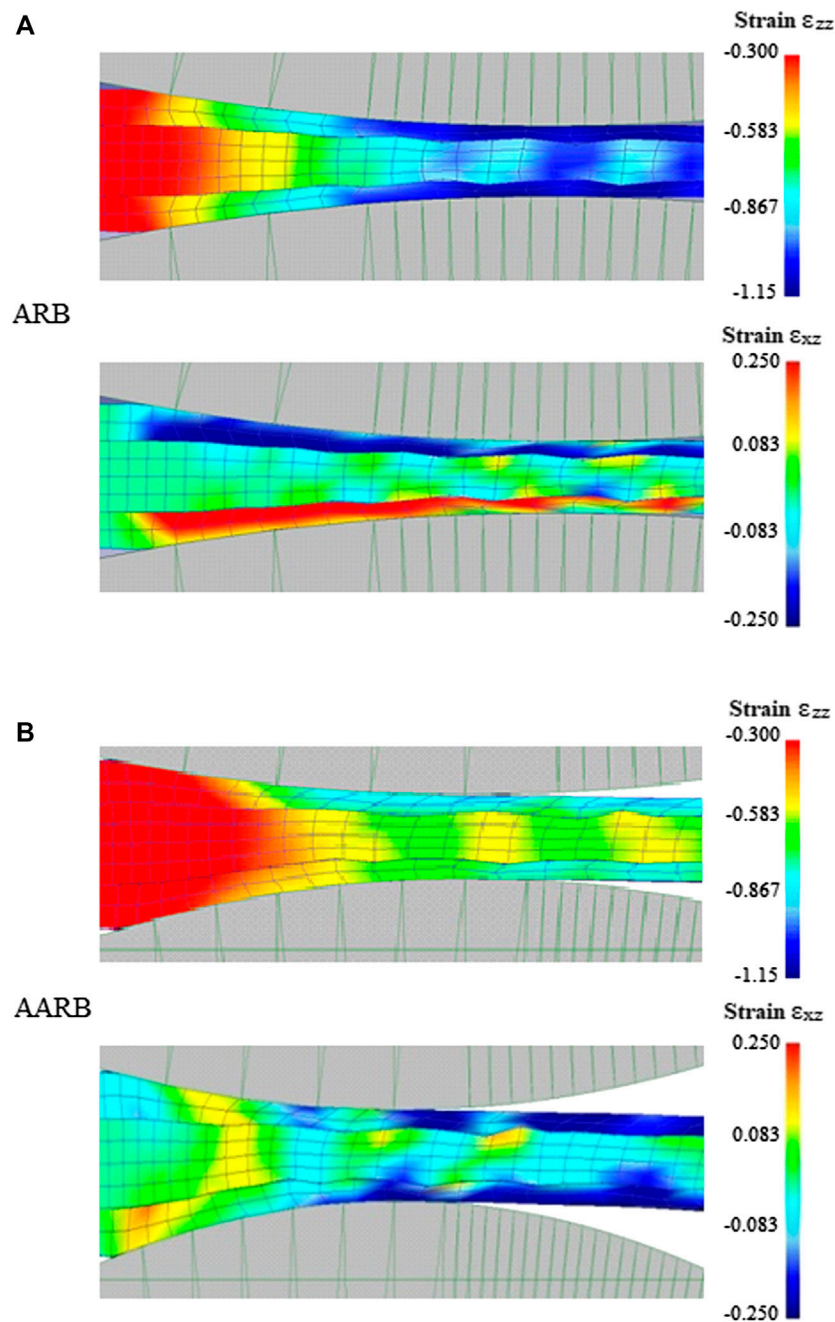


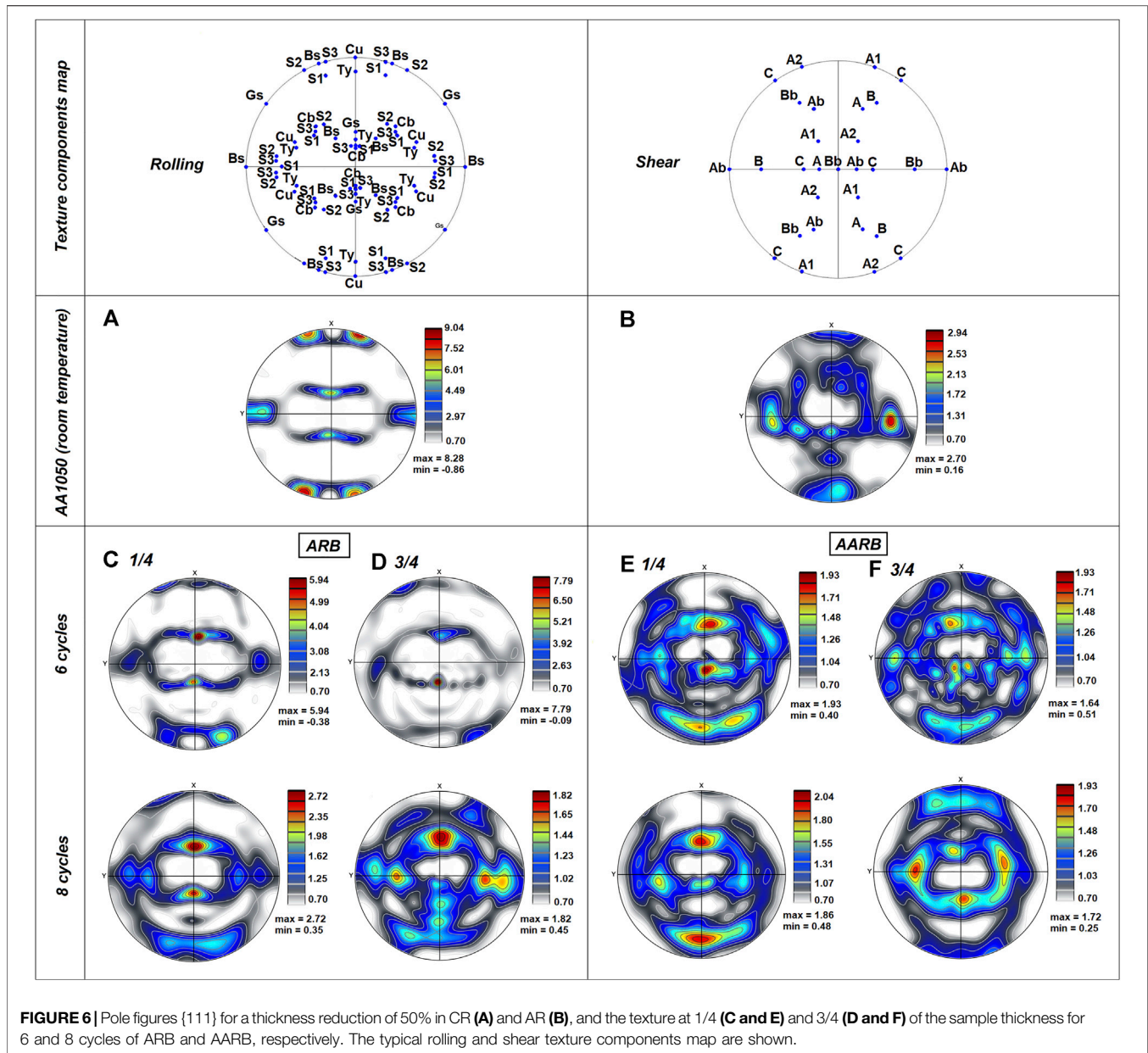
**FIGURE 5** | Strain maps simulated for the initial set of AA1050/AA7050/AA1050 layers showing compression ( $\epsilon_{zz}$ ) and shear ( $\epsilon_{xz}$ ) components in **(A)** ARB and **(B)** AARB.

$\{111\}\langle 110\rangle$ , Bb  $\{111\}\langle 112\rangle$  and the RC  $\{100\}\langle 110\rangle$  components, but it also contains compression components. **Table 2** summarizes the typical texture components and in **Figure 6** maps of the components location in the pole figures complete this information.

Because the simulation indicated that the middle interface may generate a discontinuity of shear transmission, for 6 and 8 cycles of ARB and AARB the texture was measured at 1/4 and 3/4 of the sample thickness. A characteristic was the reduction of the texture intensity as the shear and rigid body rotation were introduced due to

friction and roll's asymmetry. For the bonded samples up to 6 cycles, the ARB showed a predominance of rolling components and in AARB the shear components predominated. For 8 ARB cycles, the shear components were also present due to the formation of the macroscopic shear bands.

**Figure 7** presents a comparison with the total sum of the texture intensities of shear and rolling components. The components intensity was obtained based on integration of the component's profiles. Rolling components predominated in the symmetric



process but their intensity decreased with the number of bonding cycles. In the asymmetric process for a thickness reduction of 50%, a considerable reduction of the texture intensity was achieved, but the predominant components were still rolling. As the cycles increased the intensity of the rolling components decreased for both processes.

The composite sheets were tested in tension at room temperature and the fractured surfaces were analyzed. **Figure 8** shows the fracture surfaces at lower magnification to show the delamination at the middle layer (AA1050/AA1050 interface). Debonding at the middle interface and at poorly bonded spots was a main failure mechanism. In general, for ARB specimens the last interface was stronger in comparison with AARB specimens.

The actual efficiency of the bonding process affected the composite ductility and it was exposed when the tensile stress-

strain curves were compared in **Figure 9**. It was evident that the ARB process achieved a better interfacial adhesion at the middle interface than the AARB process. Moreover, for the ARB samples the uniform elongation was three times larger than for the AARB samples. The work-hardening rate  $\left(\frac{d\sigma}{d\epsilon} = \theta\right)$  plots are presented in **Figures 9B,C**. The ARB samples presented necking and a linear behavior in stage III. The bonding failure took place before necking for the AARB samples and early failure due to debonding was evident in the case of sample 4X AARB cycles (black arrows in **Figure 9C**). For the samples of 8 cycles, a change in the work-hardening rate was observed at the beginning of the plastic flow (indicated by blue arrows). **Table 3** summarizes the main tensile properties and KM parameters for specimens of ARB and AARB.



**TABLE 2** | Main ideal orientations along the simple shear and typical rolling orientations given by the Miller indices  $\{hkl\}\langle uvw \rangle$ .

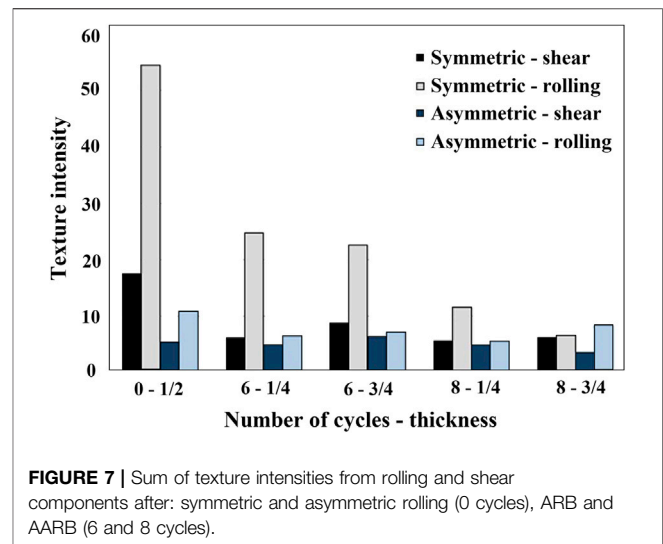
Notation	Texture component	
Rotated cube (RC)	$\{100\}\langle 110 \rangle$	Shear
A, A1, A2	$\{112\}\langle 211 \rangle, \{112\}\langle 110 \rangle$	
B, bb	$\{111\}\langle 110 \rangle, \{111\}\langle 112 \rangle$	
C	$\{011\}\langle 011 \rangle, \{011\}\langle 011 \rangle$	
A, Ab	$\{110\}\langle 112 \rangle$	
Cube (Cb)	$\{100\}\langle 001 \rangle$	Rolling
Copper (Cu)	$\{112\}\langle 111 \rangle$	
Goss (Gs)	$\{110\}\langle 001 \rangle$	
S1, S2, S3	$\{124\}\langle 211 \rangle, \{123\}\langle 412 \rangle, \{123\}\langle 634 \rangle$	
Brass (Bs)	$\{110\}\langle 112 \rangle$	
Taylor (Ty)	$\{4\ 4\ 11\}\langle 11\ 11\ 8 \rangle$	

In addition, in order to clarify the fracture mechanism and to understand the differences on the tensile behavior, SEM fracture images at higher magnification are showed in **Figure 10**. It can be seen that for 4 and 6 cycles, the two alloys have different rupture modes. The AA1050 layers presented ductile fracture with dimples and the AA7050 cleavage, which means a more fragile behavior. In addition, some debonding between AA1050 and AA7050 layers can be observed. For 8 cycles of both roll-bonding processes, the fracture of the individual layers was not apparent due to the thickness reduction, since layers are less than 7  $\mu\text{m}$  thick. Delamination and cracks between AA1050 and AA7050 layers were observed for both processes.

## DISCUSSION

The bonding experiments in this work were performed above the solvus temperature of the AA7050 alloy, which shows a remarkable amount of soluble strengthening precipitates (S, T,  $\eta$ ). These can be dissolved, coarsened and/or precipitated during the thermo-mechanical cycles, as detailed in a previous groups' work (Magalhães et al., 2020a). The final grain structure in this layer was affected by the dynamic strain aging shown in the compression experiment (see **Figure 1**) and precipitation during the cooling stage yielding a recovered structure with precipitates (see **Figure 3D**). On the other hand, the AA1050 contains a minor amount of dispersoids (~0.3 vol% of Al(Si,Fe) insoluble particles), which were not affected by the thermo-mechanical cycles. Thus, it was expected that the AA1050 experienced dynamic recovery and recrystallization phenomena, characteristic of its high stacking fault energy (SFE). This yielded an equiaxed and fine-grained structure due to continuous dynamic recrystallization (cDRX). A more complete study of the precipitation and interdiffusion experiments was published in (Magalhães et al., 2020b). The final microstructure after 8 cycles summarized in **Figure 3** showed that at 500°C, a bimodal microstructure constituted of fine grain strengthening in the AA1050 layers and precipitate strengthening in the AA7050 layers was obtained.

The use of a high friction (AARB) and a low friction (ARB) setup led to different microstructural configurations (**Figure 2**):

**FIGURE 7** | Sum of texture intensities from rolling and shear components after: symmetric and asymmetric rolling (0 cycles), ARB and AARB (6 and 8 cycles).

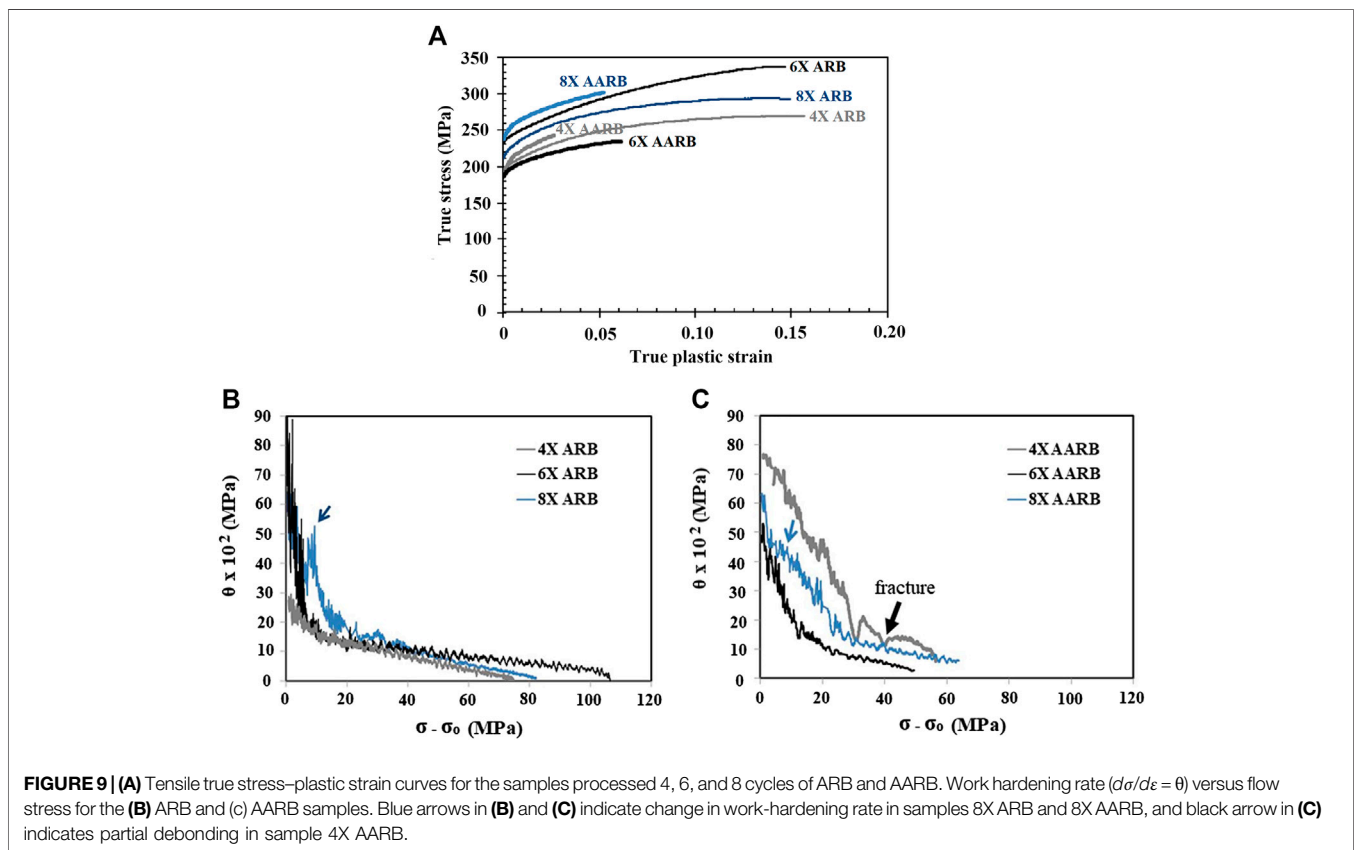
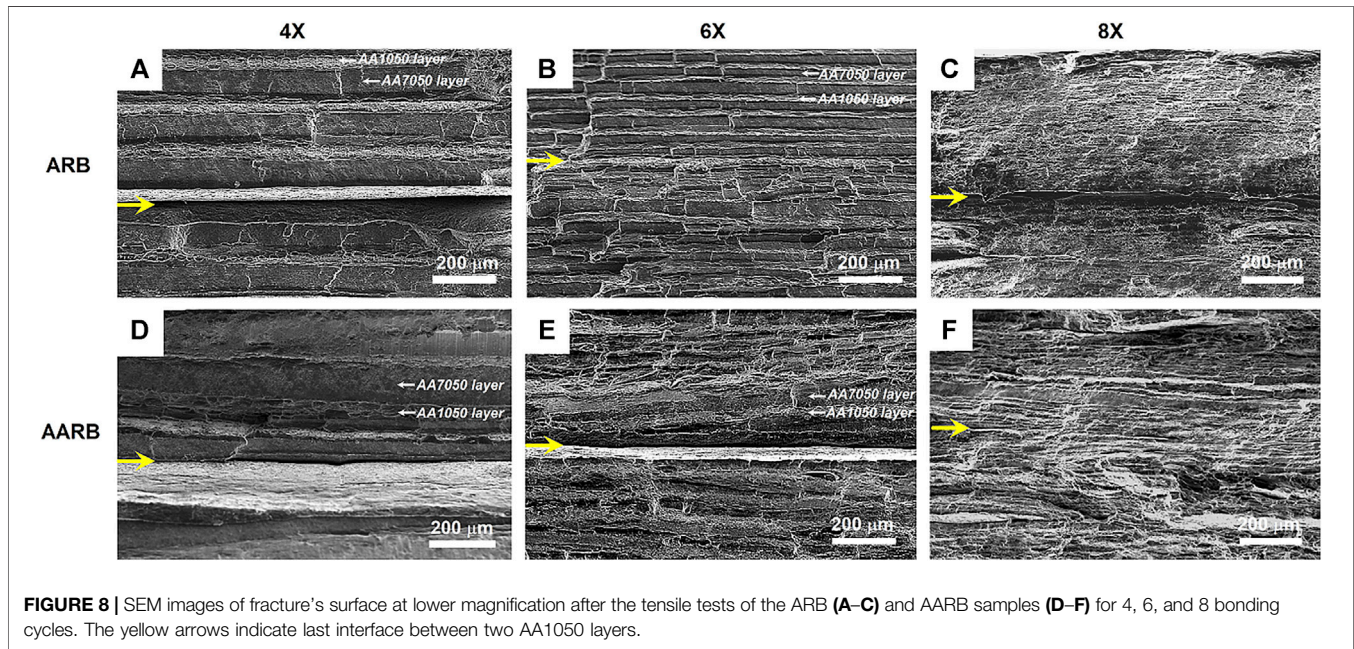
wavy and fragmented or straight layers. In the wavy-pattern structure, a composite sheet was formed by a microstructure consisting of soft layers as a matrix and harder layers as a reinforcement phase.

During the ARB of the dissimilar aluminum alloys, as pointed out by (Quadir et al., 2009); shear banding originated from the flow instability that appears in single-phase alloys at the onset of necking during the tensile test. In their work, no shear bands were formed in the solutionized Al-Sc/Al multilayered ARB, when the yield stress ratio of the two layers was of about 1.5. However, as this ratio increased over 2 after precipitation hardening, ARB resulted in a wavy-pattern. The present ARB results were also comparable to the ones published by (Mo et al., 2019b) in AA1100/AA7075 system roll-bonded at 460°C. The layers from hot ARB were straight, but when the bonded material was cold rolled, a wavy-pattern was produced. These examples show how the different work hardening behavior in solutionized/hot rolling and precipitated/cold rolling state may lead to the harder layer fragmentation. The estimated flow stresses at 500°C for the processing strain rate (**Figure 1**) show that a strain hardening ratio of about 1.5 and a hardening exponent ratio of 2 (**Table 1**) was not a sufficient condition for fragmentation.

Therefore, the wavy-pattern in this work was not caused by the difference in hardening behavior but by shear stress. The macrostructural analysis showed a small variation of the layer thicknesses in ARB, a slight formation of shear band after 6 ARB cycles, and a strong variation of the layer thicknesses plus the formation of macroscopic shear bands in AARB.

There are several possible sources of localized shear strain in the multilayer composite roll-bonding: (1) the shear strain induced by the rolls' asymmetry; (2) the shear due to interfacial friction between the rolls and sheet surface; (3) the shear due to friction at the bonding interface; and (4) the shear due to different flow behavior of the two alloys.

It is difficult to separate the first two contributions because the friction force at the roll/sheet interface is responsible for the

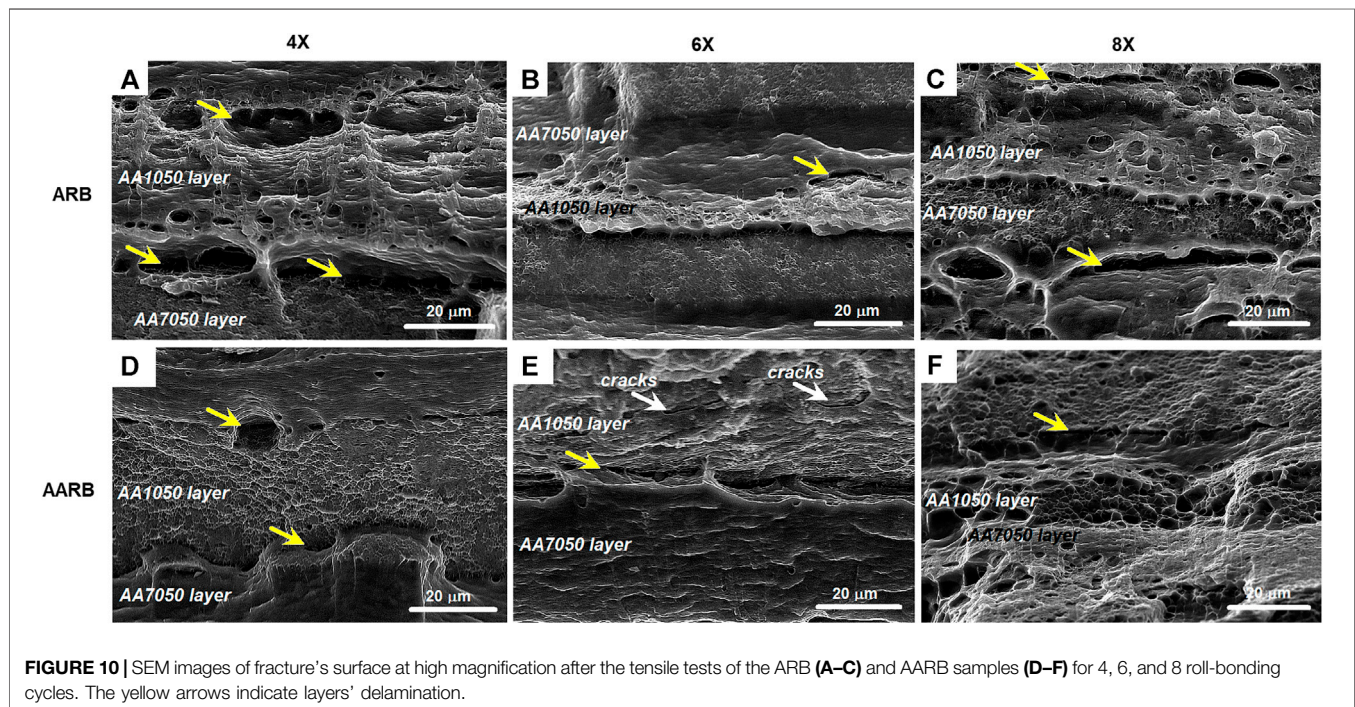


strains and speed achieved at the surfaces. From the literature on the study of asymmetric rolling (AR), it is known that the friction at the roll-sheet interface is the major contributor to the shear gradient between the top and bottom rolls. It may produce shear

deformation both in conventional rolling (CR) and AR conditions and has a much stronger effect than the asymmetry (Jin and Lloyd, 2010). The difference is that AR yields a fairly uniform shear through the thickness whereas for

**TABLE 3** | Main tensile properties and KM parameters.

Sample	Yield stress (MPa)	Ultimate tensile strength (MPa)	Uniform elongation (%)	$-[d\theta/d(\sigma-\sigma_0)]$ (MPa)	$\theta_0$ (MPa)
ARB 4X	197 ± 12	270 ± 11	15.3 ± 1.1	25.2 ± 1.9	1841 ± 121
ARB 6X	237 ± 15	338 ± 16	13.9 ± 1.2	11.9 ± 0.9	1,483 ± 135
ARB 8X	208 ± 11	277 ± 11	13.3 ± 1.0	28.1 ± 1.2	1883 ± 144
AARB 4X	185 ± 8	243 ± 12	2.4 ± 0.7	-	-
AARB 6X	190 ± 10	235 ± 19	6.3 ± 0.8	24.8 ± 1.1	1,458 ± 128
AARB 8X	237 ± 14	315 ± 10	5.3 ± 0.5	17.4 ± 1.2	1,539 ± 120

**FIGURE 10** | SEM images of fracture's surface at high magnification after the tensile tests of the ARB (A–C) and AARB samples (D–F) for 4, 6, and 8 roll-bonding cycles. The yellow arrows indicate layers' delamination.

CR, shear is concentrated in the layers close to the surface, while compression strains dominate in the center plane (Jin and Lloyd, 2007). Moreover, the increase of shear at the sheet center increased with the increment of friction (Gao et al., 2002). For ARB, the studies carried out by (Mo et al., 2019a; Li et al., 2018) showed that when ARB was applied with high friction, a wavy-pattern was also generated in hot deformation and that this was followed by an increase of shear components across the sample thickness.

The simulation results for low friction coefficient showed a small waviness of the AA1050/AA7050 interface (see Figure 5), which indicated that this instability exists, but has low intensity. When a set consisting of hard and soft alternating layers is processed by conventional rolling, a strain incompatibility is created at the interfaces. References (Wang et al., 2018; Yu et al., 2013) reported similar strain distributions as the ones presented in the simulations in this study for ARB. During rolling, the same magnitude of load is introduced to both layers separated by an interface. Because the AA1050 alloy flows to a larger strain than the AA7050 alloy, the soft layer pulls the harder layer, resulting in an in-plane shear force at the

interface. This extra shear induces rigid body rotation and reorientation components that contribute to the decrease of texture index and increment of shear character measured after six and eight cycles in the ARB experiment.

The wavy-pattern macrostructure is yielded by macroscopic shear bands (MSBs). The appearance of MSBs, as shown in Figure 2, occurred between 6 and 8 ARB cycles and are already present after 4 AARB cycles in AARB.

For high SFE metals in conventional rolling, MSBs are not a common deformation mechanism because the high recovery rate promotes a more homogeneous strain distribution, whereas in intermediate-to-low SFE the instability is caused by planar obstacles to homogeneous dislocation glide (Kong and Miszczyk, 2015). At 500°C, with alloy elements in solid solution there are fewer obstacles to the dislocation glide and although the compression experiment showed that DSA is active in the AA7050 alloy, its influence diminishes at high strain rates.

In the absence of an external shear stress (ARB), the sources of shear were the friction at the bonding interface and the slight difference of flow stress between the two alloys. Up to 6 cycles, each layer deformed individually, and the continuity was

maintained. The MSBs were generated when the AA7050 layers were thin enough (8 cycles) to work microstructurally as glide obstacles.

In the case of high friction coefficient (AARB), the shear bands were generated by the external shear stress. A previous AARB experiment with the AA1050 aluminum (de Godoi et al., 2020) showed that this process induces macroscopic shear bands due to the plastic flow, even in this high SFE material.

The MSBs present a strong tendency to grain subdivision and strain-induced re-orientation (Kong and Miszczyk, 2015). The crystal lattice rotates in such a way that one of the  $\{111\}$  slip planes became nearly parallel to the direction of maximum shear. A natural consequence of this rotation is the formation of specific MSBs texture which facilitates slip propagation across grain boundaries along the shear direction without any visible variation in the slip direction. In the ARB work of (Quadir et al., 2009) the shear band regions presented rotations around the transverse direction of all rolling texture components from  $10^\circ$  to  $20^\circ$  and the main result was the RC  $\{001\}\langle 110 \rangle$  orientation, resulting from the rotation around TD of the Cu  $\{112\}\langle 111 \rangle$  and Ty  $\{4\ 4\ 11\}\langle 11\ 11\ 8 \rangle$  textures. In the present work, the predominant effect was the reduction of texture intensity.

The present results also showed that both processes have sources of shear stress and yield low texture intensity and a mixture of shear and rolling components. The discussion above dealt with the process variables at the processing temperature, which resulted in either a continuous (ARB) or discontinuous (AARB) spatial distribution of the layers. At room temperature, besides the spatial distribution, the layers' hardness was affected by grain refinement in the AA1050 layers and by precipitates in the AA7050 layers.

An important variable in the bonding process is the adhesion at the central interface. The fracture analysis of the tensile tests showed that this surface was weaker in the AARB case. This result is in agreement with the work of (Yu et al., 2014); which tested different rolling asymmetry ratios to improve an ARB bond between AA1050 and AA6061 sheets. They concluded that there was an optimal asymmetry ratio, between 1.2 and 1.3 that increased the equivalent strain and improved the adhesion at the middle interface, while an asymmetry higher than 1.4 would deteriorate the initial bond. The asymmetry in the present study was 1.5. The simulation results in **Figure 4B** also showed that the friction coefficient may also be used to induce shear at this interface, therefore the external friction affects the adhesion at the middle interface.

The AA7050 layers are the strengthening phase in this multilayered composite and the work hardening curves showed that the hardening behavior was controlled by this macrostructural constituent. Necking and fragmentation of this layer reduces the ductility because stress concentrates at these points, and is in accordance with other results in the literature (Govindaraj et al., 2013; Chen et al., 2014; Chen and Chen, 2015).

More specifically, (Chen et al., 2014) studied the same class of alloys used in this work, and observed that yield strength, tensile strength, and elongation decreased with the increase of variation of interface shape when the number of layers was

kept constant. When the scale was reduced, in other words, decreasing the layer thickness below  $6\ \mu\text{m}$  (Chen and Chen, 2015), the different layers interacted with the dislocation glide process and an increase in yield stress and elongation was observed. This is similar to the case of 8 cycles in both processes in present work. Concerning to the ductility differences in **Figures 9B,C**, it can be observed that the uniform elongation was nearly three times larger for ARB than for the AARB samples. There are two factors contributing to this behavior. The first is associated to a better interfacial adhesion at the interfaces achieved during ARB that results in less delaminated layers, as shown in **Figures 8** and **10**. The second is the thickness and shape of the AA7050 layers, that act as load bearing constituent, controlling the fracture. The wavy-pattern achieved in the AARB produced layers necked in several regions, in which the strain concentrates during tensile tests. The consequence is that the fracture occurs earlier in the AA7050 layers of the composite sheets produced by AARB, in comparison with ARB sheets that maintain straight layers up to 6 cycles.

Since AA7050 layers control the mechanical response, it is worth noting that the final microstructure after ARB or AARB are different in these layers. As shown in **Figure 3D**, a precipitate coarsening takes place in the AA7050 layers of the AARB sheets mainly at the grain boundaries, while for sheets processed by ARB, it can be observed a fine precipitate dispersion that contributed to the strength.

In **Figures 9B,C**, the work-hardening rate changed due to two main factors: the storage of geometrically necessary dislocations, and the obstacles represented by dense regions of non-shearable precipitates, since AA7050 layers containing a high density of overaged particles (S, T,  $\eta$ ) (Dumont et al., 2003). For 4X and 6X sheets, for both ARB and AARB, the KM plots presents a linear slope at the stage III, characteristic of the process dominated by dislocation glide and recovery. In contrast, 8X sheets presented a non-linear behavior indicated by the abrupt change in the work-hardening rate (see blue arrows in **Figures 9B,C**), which is associated to the presence of non-shearable particles. The main consequence is an accumulation of Orowan loops around these precipitates causing the activation of bypassing mechanisms for dislocation movement (Fribourg et al., 2011).

In summary, the present results showed that the external friction and asymmetry of the fabrication process had a strong influence on the macrostructural pattern and in the final mechanical response of multilayered composite sheets. Thus, the ARB was able to produce multilayered composite sheets of AA1050/AA7050 with enhanced strength and elongation, in comparison with AARB route.

## CONCLUSION

In this work was investigate the influence of external shear and friction on the macrostructural pattern formation and final tensile properties during accumulative roll-bonding of two dissimilar aluminum alloys. The results may be summarized as follows:

- i. From numerical simulations of high friction and high roll asymmetry (AARB), it was observed that the central layer accumulates half the strain than the softer layers, which resulted in a shear gradient at the central layer and both roll-sheet interfaces, yielding a wavy-pattern configuration due to the formation of macroscopic shear bands. For the low friction and symmetric rolling (ARB), the main variation of shear strain was found at the layer interface, but it concentrated in the AA1050 layer, which resulted in a straight-pattern up to 6 cycles. After 8 ARB cycles, some macroscopic shear bands were observed.
- ii. For AARB sheets it was observed a reduction of the texture intensity, since the shear and rigid body rotation were introduced due to friction and roll's asymmetry.
- iii. ARB sheets showed a predominance of rolling components up to 6 cycles. After 8 ARB cycles, the shear components were also present due to the formation of the macroscopic shear bands. The texture intensity decreased with the increment of bonding cycles.
- iv. After roll-bonding at 500°C, a macrostructure of wavy-pattern was achieved for AARB sheets, while a straight-pattern with some macroscopic shear bands was observed for ARB sheets. At microstructure level, a bimodal structure was achieved in both roll-bonding processes, constituted of equiaxed structure in the AA1050 layers and fine-grained and precipitate strengthening in the AA7050 layers.
- v. The ARB sheets presented higher strength and ductility in comparison to the AARB sheets. The interfacial adhesion for ARB sheets was stronger than AARB, which contributed to the ductility. In addition, AA7050 layers act as load bearing constituent, thus the fragmentation and necking during AARB resulted in earlier fracture and lower ductility.

These findings indicate that ARB is suitable to produce AA1050/AA7050 multilayer composite sheets with a great combination of strength and ductility.

## DATA AVAILABILITY STATEMENT

The raw data supporting the conclusions of this article will be made available by the authors, without undue reservation.

## AUTHOR CONTRIBUTIONS

DM Conceptualization, Investigation, Formal analysis, Writing—original draft. OC Investigation. JR Methodology, Software. VS Resources, Writing—review and editing. AK Conceptualization, Formal analysis, Writing—review and editing, Project administration.

## FUNDING

We gratefully acknowledge the financial support from the National Council for Scientific and Technological Development—CNPq (Grant Numbers 153585/2018-8 and 160274/2019-2) and the Coordination for the Improvement of Higher Education Personnel (CAPES)—Finance Code 001 and the Graduate Program in Materials Science and Engineering from the Federal University of São Carlos. The authors would like to thank the Brazilian Nanotechnology National Laboratory LNNano for allowing us to use its X-ray diffractometer.

## REFERENCES

- Abo-Elkhier, M. (2004). Modeling of high-temperature deformation of commercial pure aluminum (1050). *J. Mater. Eng. Perform.* 13(2), 241–247. doi:10.1361/10599490418280
- Anne, G., Ramesh, M. R., Shivananda Nayaka, H., Arya, S. B., and Sahu, S. (2017). Microstructure evolution and mechanical and corrosion behavior of accumulative roll bonded Mg-2%Zn/Al-7075 multilayered composite. *J. Mater. Eng. Perform.* 26(4), 1726–1734. doi:10.1007/s11665-017-2576-z
- Beausir, B., and Fundenberger, J.-J. (2017). *Analysis tools for electron and X-ray diffraction, ATEX—software*. Metz, Université de Lorraine.
- Chen, G., Ren, C., Ke, Z., Li, J., and Yang, X. (2016). Modeling of flow behavior for 7050-T7451 aluminum alloy considering microstructural evolution over a wide range of strain rates. *Mech. Mater.* 95, 146–157. doi:10.1016/j.mechmat.2016.01.006
- Chen, Z., and Chen, Q. (2015). Interface shear actions and mechanical properties of nanostructured dissimilar Al alloy laminated metal composites. *J. Nanomater.* 2015, 612029. doi:10.1155/2015/612029
- Chen, Z., Wu, X., Hu, H., Chen, Q., and Liu, Q. (2014). Effect of individual layer shape on the mechanical properties of dissimilar Al alloys laminated metal composite sheets. *J. Mater. Eng. Perform.* 23(3), 990–1001. doi:10.1007/s11665-013-0804-8
- de Godoi, R. P., Camilo Magalhães, D. C., Avalos, M., Bolmaro, R. E., Sordi, V. L., and Kliuga, A. M. (2020). Microstructure, texture and interface integrity in sheets processed by asymmetric accumulative roll-bonding. *Mater. Sci. Eng.* 771, 138634. doi:10.1016/j.msea.2019.138634
- Dumont, D., Deschamps, A., and Brechet, Y. (2003). On the relationship between microstructure, strength and toughness in AA7050 aluminum alloy. *Mater. Sci. Eng.* 356(1), 326–336. doi:10.1016/S0921-5093(03)00145-X
- Ebrahimi, S. H. S., Deghani, K., Aghazadeh, J., Ghasemian, M. B., and Zangeneh, S. (2018). Investigation on microstructure and mechanical properties of Al/Al-Zn-Mg-Cu laminated composite fabricated by accumulative roll bonding (ARB) process. *Mater. Sci. Eng.* 718, 311–320. doi:10.1016/j.msea.2018.01.130
- Fattah-Alhosseini, A., Naseri, M., and Alemi, M. H. (2017). Effect of particles content on microstructure, mechanical properties, and electrochemical behavior of aluminum-based hybrid composite processed by accumulative roll bonding process. *Metall. Mater. Trans.* 48(3), 1343–1354. doi:10.1007/s11661-016-3933-5
- Fribourg, G., Bréchet, Y., Deschamps, A., and Simar, A. (2011). Microstructure-based modelling of isotropic and kinematic strain hardening in a precipitation-hardened aluminium alloy. *Acta Mater.* 59(9), 3621–3635. doi:10.1016/j.actamat.2011.02.035
- Gao, H., Ramalingam, S. C., Barber, G. C., and Chen, G. (2002). Analysis of asymmetrical cold rolling with varying coefficients of friction. *J. Mater. Process. Technol.* 124(1), 178–182. doi:10.1016/S0924-0136(02)00131-0
- Govindaraj, N. V., Frydendahl, J. G., and Holmedal, B. (2013). Layer continuity in accumulative roll bonding of dissimilar material combinations. *Mater. Des.* 52, 905–915. doi:10.1016/j.matdes.2013.06.031
- Höppel, H. W., Korn, M., Lapovok, R., and Mughrabi, H. (2010). Bimodal grain size distributions in UFG materials produced by SPD: their evolution and effect on mechanical properties. *J. Phys. Conf.* 240, 012147. doi:10.1088/1742-6596/240/1/012147

- Huang, C. X., Hu, W. P., Wang, Q. Y., Wang, C., Yang, G., and Zhu, Y. T. (2015). An ideal ultrafine-grained structure for high strength and high ductility. *Mater. Res. Lett.* 3(2), 88–94. doi:10.1080/21663831.2014.968680
- Jamaati, R., and Toroghinejad, M. R. (2011). Cold roll bonding bond strengths: review. *Mater. Sci. Technol.* 27(7), 1101–1108. doi:10.1179/026708310X12815992418256
- Jin, H., and Lloyd, D. J. (2007). Evolution of texture in AA6111 aluminum alloy after asymmetric rolling with various velocity ratios between top and bottom rolls. *Mater. Sci. Eng.* 465(1), 267–273. doi:10.1016/j.msea.2007.02.128
- Jin, H., and Lloyd, D. J. (2010). The different effects of asymmetric rolling and surface friction on formation of shear texture in aluminium alloy AA5754. *Mater. Sci. Technol.* 26(6), 754–760. doi:10.1179/174328409X405634
- Kong, H., and Miszczyk, M. M. (2015). Deformation microstructure and texture transformations in FCC metals of medium-to-high stacking fault energy: critical role of micro- and macro-scale shear bands. *Arch. Metall. Mater.* 3, 44–59. doi:10.1016/s1359-6454(00)00050-1
- Kulagin, R., Beygelzimer, Y., Bachmaier, A., Pippan, R., and Estrin, Y. (2019). Benefits of pattern formation by severe plastic deformation. *Appl. Mater. Today* 15, 236–241. doi:10.1016/j.apmt.2019.02.007
- Kumar, P., Kawasaki, M., and Langdon, T. G. (2016). Review: overcoming the paradox of strength and ductility in ultrafine-grained materials at low temperatures. *J. Mater. Sci.* 51(1), 7–18. doi:10.1007/s10853-015-9143-5
- Li, L., Nagai, K., and Yin, F. (2008). Progress in cold roll bonding of metals. *Sci. Technol. Adv. Mater.* 9(2), 023001. doi:10.1088/1468-6996/9/2/023001
- Li, S., Yang, L., and Qin, N. (2018). Development of through-thickness texture gradient and persistence of shear-type textures during annealing of commercial purity aluminium sheet processed by accumulative roll-bonding. *J. Mater. Sci. Technol.* 34(5), 821–831. doi:10.1016/j.jmst.2017.04.019
- Magalhães, D. C. C., Cintho, O. M., Rubert, J. B., Sordi, V. L., and Kliauga, A. M. (2020a). The role of shear strain during Accumulative Roll-Bonding of multilayered composite sheets: pattern formation, microstructure and texture evolution. *Mater. Sci. Eng.* 14, 140055. doi:10.1016/j.msea.2020.140055
- Magalhães, D. C. C., Sordi, V. L., and Kliauga, A. M. (2020b). Microstructure evolution of multilayered composite sheets of AA1050/AA7050 Al alloys produced by Asymmetric Accumulative Roll-Bonding. *Mater. Char.* 162, 110226. doi:10.1016/j.matchar.2020.110226
- Mendes, A., Timokhina, I., Molotnikov, A., Hodgson, P. D., and Lapovok, R. (2017). Role of shear in interface formation of aluminium-steel multilayered composite sheets. *Mater. Sci. Eng.* 705, 142–152. doi:10.1016/j.msea.2017.08.025
- Mi, H., Shi, Q. N., Wang, J. L., Zhou, L., and Chen, L. W. (2011). Effect of asymmetrical accumulative roll-bonding and heat treatment on the formation of ultra-fine twin copper. *Mater. Sci. Forum* 667–669, 611–616. doi:10.4028/www.scientific.net/MSF
- Mo, T., Chen, Z., Huang, H., Lin, J., and Liu, Q. (2019a). Effect of two-step annealing on recrystallized structure and mechanical properties in AA7075/AA1100 laminated metal composites processed by accumulative roll bonding. *Mater. Char.* 158, 109951. doi:10.1016/j.matchar.2019.109951
- Mo, T. Q., Chen, Z. J., Li, B. X., Wang, P. J., and Liu, Q. (2019b). Tailoring of interface structure and mechanical properties in ARBed 1100/7075 laminated composites by cold rolling. *Mater. Sci. Eng.* 755, 97–105. doi:10.1016/j.msea.2019.03.075
- Naseri, M., Reihanian, M., and Borhani, E. (2016). A new strategy to simultaneous increase in the strength and ductility of AA2024 alloy via accumulative roll bonding (ARB). *Mater. Sci. Eng.* 656, 12–20. doi:10.1016/j.msea.2016.01.020
- Ng, H. P., Przybilla, T., Schmidt, C., Lapovok, R., Orlov, D., Höppel, H.-W., et al. (2013). Asymmetric accumulative roll bonding of aluminium–titanium composite sheets. *Mater. Sci. Eng.* 576, 306–315. doi:10.1016/j.msea.2013.04.027
- Quadir, M. Z., Ferry, M., Al-Buhamad, O., and Munroe, P. R. (2009). Shear banding and recrystallization texture development in a multilayered Al alloy sheet produced by accumulative roll bonding. *Acta Mater.* 57(1), 29–40. doi:10.1016/j.actamat.2008.08.056
- Rahmatbadi, D., Hashemi, R., Mohammadi, B., and Shojaei, T. (2017). Experimental evaluation of the plane stress fracture toughness for ultra-fine grained aluminum specimens prepared by accumulative roll bonding process. *Mater. Sci. Eng.* 708, 301–310. doi:10.1016/j.msea.2017.09.085
- Rahmatbadi, D., Tayyebi, M., Sheikhi, A., and Hashemi, R. (2018). Fracture toughness investigation of Al1050/Cu/MgAZ31ZB multi-layered composite produced by accumulative roll bonding process. *Mater. Sci. Eng.* 734, 427–436. doi:10.1016/j.msea.2018.08.017
- Reihanian, M., and Naseri, M. (2016). An analytical approach for necking and fracture of hard layer during accumulative roll bonding (ARB) of metallic multilayer. *Mater. Des.* 89, 1213–1222. doi:10.1016/j.matdes.2015.10.088
- Rometsch, P. A., Zhang, Y., and Knight, S. (2014). Heat treatment of 7xxx series aluminium alloys—some recent developments. *Trans. Nonferrous Metals Soc. China* 24(7), 2003–2017. doi:10.1016/S1003-6326(14)63306-9
- Ruppert, M., Böhm, W., Nguyen, H., Höppel, H. W., Merklein, M., and Göken, M. (2013). Influence of upscaling accumulative roll bonding on the homogeneity and mechanical properties of AA1050A. *J. Mater. Sci.* 48(24), 8377–8385. doi:10.1007/s10853-013-7648-3
- Samaee, M., Najafi, S., Eivani, A. R., Jafarian, H. R., and Zhou, J. (2016). Simultaneous improvements of the strength and ductility of fine-grained AA6063 alloy with increasing number of ECAP passes. *Mater. Sci. Eng.* 669, 350–357. doi:10.1016/j.msea.2016.05.070
- Sidor, J., Miroux, A., Petrov, R., and Kestens, L. (2008). Microstructural and crystallographic aspects of conventional and asymmetric rolling processes. *Acta Mater.* 56(11), 2495–2507. doi:10.1016/j.actamat.2008.01.042
- Su, L., Lu, C., Tieu, A. K., Deng, G., and Sun, X. (2013). Ultrafine grained AA1050/AA6061 composite produced by accumulative roll bonding. *Mater. Sci. Eng.* 559, 345–351. doi:10.1016/j.msea.2012.08.109
- Tsuji, N., Saito, Y., Lee, S.-H., and Minamino, Y. (2003). ARB (accumulative roll-bonding) and other new techniques to produce bulk ultrafine grained materials. *Adv. Eng. Mater.* 5(5), 338–344. doi:10.1002/adem.200310077
- Valiev, R. Z. (2004). Paradoxes of severe plastic deformation. *Nanomater. Severe Plast. Deform.* 19, 107–117. doi:10.1002/9781118357002.ch92
- Wang, H., Su, L., Yu, H., Lu, C., Tieu, A. K., Liu, Y., et al. (2018). A new finite element model for multi-cycle accumulative roll-bonding process and experiment verification. *Mater. Sci. Eng.* 726, 93–101. doi:10.1016/j.msea.2018.04.040
- Wang, J.-L., Xu, R.-d., Wang, S.-h., Qian, T.-c., and Shi, Q.-n. (2012). Formation mechanism and organizational controlling of ultra-fine-grain copper processed by asymmetrical accumulative rolling-bond and annealing. *Trans. Nonferrous Metals Soc. China* 22(11), 2672–2678. doi:10.1016/S1003-6326(11)61516-1
- Wang, Y. M., and Ma, E. (2004). Three strategies to achieve uniform tensile deformation in a nanostructured metal. *Acta Mater.* 52(6), 1699–1709. doi:10.1016/j.actamat.2003.12.022
- Wierzbka, A., Mróz, S., Szota, P., Stefanik, A., and Mola, R. (2015). The influence of the asymmetric arb process on the properties of Al-Mg-Al multi-layer sheets/Wpływ asymetrii W Procesie arb Na Właściwości Wielowarstwowych blach Al-Mg-Al. *Arch. Metall. Mater.* 7, 23–76. doi:10.1103/physrevb.79.224103
- Yazar, Ö., Ediz, T., and Öztürk, T. (2005). Control of macrostructure in deformation processing of metal/metal laminates. *Acta Mater.* 53(2), 375–381. doi:10.1016/j.actamat.2004.09.033
- Yu, H., Lu, C., Tieu, A. K., Godbole, A., Su, L., Sun, Y., et al. (2013). Fabrication of ultra-thin nanostructured bimetallic foils by accumulative roll bonding and asymmetric rolling. *Sci. Rep.* 3(1), 2373. doi:10.1038/srep02373
- Yu, H., Tieu, A. K., Lu, C., and Godbole, A. (2014). An investigation of interface bonding of bimetallic foils by combined accumulative roll bonding and asymmetric rolling techniques. *Metall. Mater. Trans.* 45(9), 4038–4045. doi:10.1007/s11661-014-2311-4
- Zhao, Y.-H., Bingert, J. F., Liao, X.-Z., Cui, B.-Z., Han, K., Sergueeva, A. V., et al. (2006). Simultaneously increasing the ductility and strength of ultra-fine-grained pure copper. *Adv. Mater.* 18(22), 2949–2953. doi:10.1002/adma.200601472

**Conflict of Interest:** The authors declare that the research was conducted in the absence of any commercial or financial relationships that could be construed as a potential conflict of interest.

Copyright © 2020 Magalhães, Rubert, Cintho, Sordi and Kliauga. This is an open-access article distributed under the terms of the Creative Commons Attribution License (CC BY). The use, distribution or reproduction in other forums is permitted, provided the original author(s) and the copyright owner(s) are credited and that the original publication in this journal is cited, in accordance with accepted academic practice. No use, distribution or reproduction is permitted which does not comply with these terms.